Quantum Signatures in Quench from Chaos to Superradiance

Sayak Ray,[1,2] Amichay Vardi,[1] and Doron Cohen[3]
[1]*Department of Chemistry, Ben-Gurion University of the Negev, Beer-Sheva 84105, Israel*
[2]*Physikalisches Institut, Rheinische Friedrich-Wilhelms-Universität Bonn, Nußallee 12, 53115 Bonn, Germany*
[3]*Department of Physics, Ben-Gurion University of the Negev, Beer-Sheva 84105, Israel*

(Received 19 January 2022; accepted 10 March 2022; published 1 April 2022)

The driven-dissipative Dicke model features normal, superradiant, and lasing steady states that may be regular or chaotic. We report quantum signatures of chaos in a quench protocol from the lasing states. Within the framework of a classical mean-field perspective, once quenched, the system relaxes either to the normal or to the superradiant state. Quench from chaos, unlike quench from a regular lasing state, exhibits erratic dependence on control parameters. In the quantum domain, this sensitivity implies an effect that is similar to universal conductance fluctuations.

DOI: 10.1103/PhysRevLett.128.130604

The essence of chaos is often presented as a "butterfly effect": a small variation in a control parameter h leads to a drastically different outcome, with seemingly erratic deterministic dependence. For example, a particle is launched into a chaotic cavity and is either transmitted ($Q = 1$) or reflected ($Q = 0$). The classical dependence $Q(h)$ looks uncorrelated on a scale that is larger than some exponentially small δh_c. Alternatively, one may consider a "coin tossing" experiment that involves a dissipative quench to the binary final outcome due to the proverbial coin-ground interaction.

In the present Letter, we consider a "quench from chaos" (QFC) to bistability for atoms in a lasing cavity. The control parameter h is a prequench preparation time $t_{\rm prep}$, and the postquench outcome is either a normal state (NS) [$Q = 0$] or a superradiant (SR) state [$Q \neq 0$]. The observable Q is the number of photons in the cavity, namely, $Q = n(t_m)$ where t_m is the time to measurement, i.e., the duration of the quench. Within the framework of a classical (mean-field) perspective, for an appropriate tuning of the atom-field interaction, the dependence of Q on h is erratic, as illustrated in Fig. 1. We seek for the signature of this dependence in the quantum regime.

The simplest quantum version of QFC is a semiclassical phase-space picture. The wave packet spreads over the chaotic sea, and therefore the erratic dependence of $\mathrm{Prob}(Q = 1)$ on h is smeared away: in the *classical* mean-field context this probability is either 0% or 100%, while in the *semiclassical* truncated Wigner approximation perspective it equals a number p that reflects the relative volume of the basin leading to the SR state. However, interference between semiclassical trajectories should result in irregular dependence on h in the exact *quantum* many-body dynamics, see Fig. 1.

Fluctuations due to QFC are analogous to universal conductance fluctuations (UCFs) [1,2] and chaos-assisted tunneling (CAT) [3]. In the UCF context, Q is the transmission (conductance) through a chaotic cavity, and h is the magnetic field, while in the CAT context, Q is the tunneling rate, and h is the scaled Planck constant. In all those cases (QFC, UCFs, CAT) the systematic *nonsemiclassical* fluctuations in the output signal constitute quantum signature of chaos. However, in QFC we have the extra complication due to dissipation, and one wonders whether any memory of chaos survives after the quench. The availability of both regular and chaotic lasing steady states in the driven-dissipative Dicke model [4–12] offers an opportunity to directly contrast the QFC with a quench from a quasiperiodic regular orbit and show how the h dependence of the quench outcome indicates whether the prepared state was regular or chaotic.

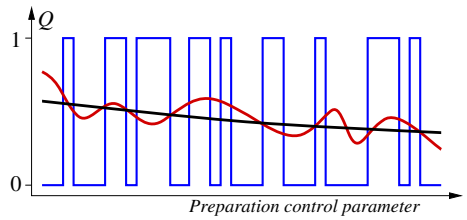

FIG. 1. Quantum fluctuations in QFC. In the classical (mean-field) limit, the outcome of the measurement (blue line) is binary and erratically depends on the parameter that controls the preparation protocol (in our demonstration it is the preparation time $t_{\rm prep}$). In the semiclassical (truncated Wigner) approximation, this erratic dependence is smoothed away (black line). The measured $\langle Q \rangle$ reflects the relative volume of the basin that leads to the $Q = 1$ attractor. In the proper quantum treatment, the outcome (red line) manifests fluctuations that arise from interference of trajectories. However, any *mesoscopic* system eventually relaxes, such that for $t = \infty$ the expectation value $\langle Q \rangle$ reflects a thermal equilibrium that does not depend on the initial preparation.

Outline.—We first review the regime diagram of the dissipative Dicke model, highlighting NS, SR, and regular and chaotic lasing regions. Relaxation toward the NS-SR bistability is then considered as a measurement protocol. In the full QFC scheme, we choose the prequench preparation time ($t_{\rm prep}$) as a control parameter. This QFC scenario is contrasted with the quench from dynamically regular motion. In particular, we aim to clarify the significance of the quench duration (t_m).

The Dicke model.—The model describes N two level atoms (excitation energy $\mathcal{E}$) that interact with a single cavity mode (frequency Ω) [13,14]. The Hamiltonian involves, respectively, the bosonic field operator $\hat{a}$ and the Pauli matrices $\hat{\sigma}_i$, with the common subscripts $i = x, y, z, \pm$. The couplings g and $\tilde{g}$ denote the strength of the corotating and counterrotating terms of atom-photon interaction. Namely,

$$\hat{H}_D = \Omega\hat{a}^\dagger\hat{a} + \frac{\mathcal{E}}{2}\sum_{r=1}^{N}\hat{\sigma}_z^r + \frac{g}{\sqrt{N}}\sum_{r=1}^{N}(\hat{\sigma}_+^r\hat{a} + \hat{\sigma}_-^r\hat{a}^\dagger) + \frac{\tilde{g}}{\sqrt{N}}\sum_{r=1}^{N}(\hat{\sigma}_-^r\hat{a} + \hat{\sigma}_+^r\hat{a}^\dagger). \quad (1)$$

We define the mode occupation operator $\hat{n} = \hat{a}^\dagger\hat{a}$ and the collective excitation operators $\hat{S}_i^\ell = (1/2)\sum_r \hat{\sigma}_i^r$, $(i = x, y, z)$ that generate a spin algebra with angular momentum $\ell \le N/2$.

It is well known [14–17] that the ground state of the Dicke model undergoes a quantum phase transition from a NS with $\langle n\rangle = 0$ to a pair of SR states with $\langle n\rangle \neq 0$. Moreover, depending on $(g, \tilde{g})$, the model exhibits an excited state quantum phase transition [18,19].

Dissipative dynamics.—Several loss and incoherent processes are associated with the Dicke system [5–12]. The corresponding dissipative dynamics can be studied within the framework of a Lindblad master equation,

$$\dot{\rho} = -i[\hat{H}_D, \rho] + \kappa\mathcal{L}[\hat{a}] + \sum_{r=1}^{N}(\gamma_\downarrow\mathcal{L}[\hat{\sigma}_-^r] + \gamma_\uparrow\mathcal{L}[\hat{\sigma}_+^r]) + \frac{1}{N}\sum_{\ell}^{N/2}(\gamma_\downarrow^c\mathcal{L}[\hat{S}_-^\ell] + \gamma_\uparrow^c\mathcal{L}[\hat{S}_+^\ell]), \quad (2)$$

where $\mathcal{L}[\hat{\mathcal{O}}] \equiv \hat{\mathcal{O}}\rho\hat{\mathcal{O}}^\dagger - \frac{1}{2}(\hat{\mathcal{O}}^\dagger\hat{\mathcal{O}}\rho + \rho\hat{\mathcal{O}}^\dagger\hat{\mathcal{O}})$. The incoherent dynamics in Eq. (2) arises from the cavity-photon loss $\mathcal{L}[\hat{a}]$ with a rate κ and from local incoherent decay and pumping transitions $\mathcal{L}[\hat{\sigma}_-^r]$ and $\mathcal{L}[\hat{\sigma}_+^r]$ with rates $\gamma_\downarrow$ and $\gamma_\uparrow$, respectively. Apart from the local incoherent processes, there are also incoherent collective processes $\mathcal{L}[\hat{S}_-^\ell]$ and $\mathcal{L}[\hat{S}_+^\ell]$, with rates $\gamma_\downarrow^c$ and $\gamma_\uparrow^c$, respectively. Below, we focus on collective incoherent transitions and neglect local incoherent processes. The collective decay and pumping for the Dicke model is justified when the atoms are concentrated in a spatial region much smaller than the wavelength of the coupled cavity modes [5]. The total spin ℓ then becomes a constant of motion. Per our preparation, we focus on the $\ell = N/2$ multiplet. The reduced Hamiltonian can be written in terms of the $\hat{S}_i$ operators. For large N the classical approximation is obtained by treating them as classical coordinates. We define scaled variables $s \coloneqq \hat{S}_-/N$ and $s_{x,y,z} \coloneqq \hat{S}_{x,y,z}/N$, such that $s_x^2 + s_y^2 + s_z^2 = 1/4$. We also scale the bosonic coordinates as $a \coloneqq \hat{a}/\sqrt{N}$. Consequently, the classical equations of motion are

$$\begin{aligned}\dot{a} &= -(i\Omega + \kappa/2)a - i(gs + \tilde{g}s^*),\\ \dot{s} &= -(i\mathcal{E} + f_c s_z)s + 2i(ga + \tilde{g}a^*)s_z,\\ \dot{s}_z &= f_c|s|^2 - i[g(as^* - a^*s) + \tilde{g}(a^*s^* - as)],\end{aligned} \quad (3)$$

where the net incoherent pumping is $f_c = \gamma_\uparrow^c - \gamma_\downarrow^c$, while the total incoherent rate of transition is $\gamma_c = \gamma_\uparrow^c + \gamma_\downarrow^c$. In Fig. 2 we present phase diagrams obtained by stability analysis and numerical long-time propagation of Eq. (3). The phase diagram includes NS and SR, as well as regular and chaotic lasing phases. Moreover, there is a bistable NS-SR phase that we are going to utilize for the measurement protocol.

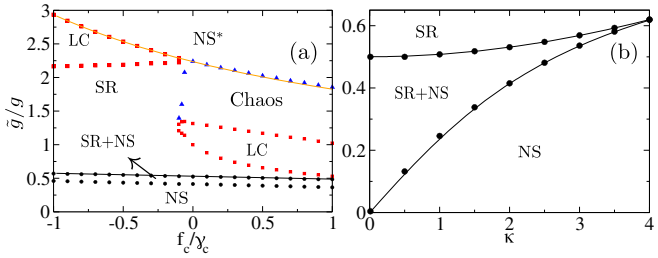

FIG. 2. Steady-state phase diagram. The vertical axis is the $\tilde{g}/g$ ratio that reflects coherent pumping. In (a) the horizontal axis is the normalized incoherent collective pumping. We assume $\Omega = \mathcal{E} = 1$ and $g = 2$, while $\kappa = 2$ and $\gamma_c = 0.5$. The label NS* indicates a stable all-atom-excited state. The labels "LC" and "Chaos" indicate a regular limit cycle and a chaotic lasing state, respectively. With vanishing dissipation, bistability appears for $\tilde{g}/g \le 0.5$, and the energy landscape has three attractors (NS and two SR fixed points), while with finite dissipation this range is shifted. (b) Dependence of the bistability region on κ, for $g = 2$, while $f_c = \gamma_c = 0$. The symbols are based on numerical analysis, while the lines are based on stability analysis (see Supplemental Material [20]).

The NS-SR bistability.—An energy landscape $E(n, s_z)$ for the cavity can be obtained by minimizing H_D for a given (n, s_z) under the constraint $s_x^2 + s_y^2 + s_z^2 = 1/4$, see Supplemental Material [20]. For small g this landscape exhibits a stable NS minimum at $n = 0$ and $s_z = -1/2$ that becomes an attractor for $\kappa > 0$. For $(g + \tilde{g}) > \sqrt{\Omega\mathcal{E}}$, the NS becomes an energetic saddle point rather than a local minimum, but if $\tilde{g}/g < 1 - [\sqrt{\Omega\mathcal{E}}/g]$ it maintains dynamical stability and remains an attractor. The transition of the

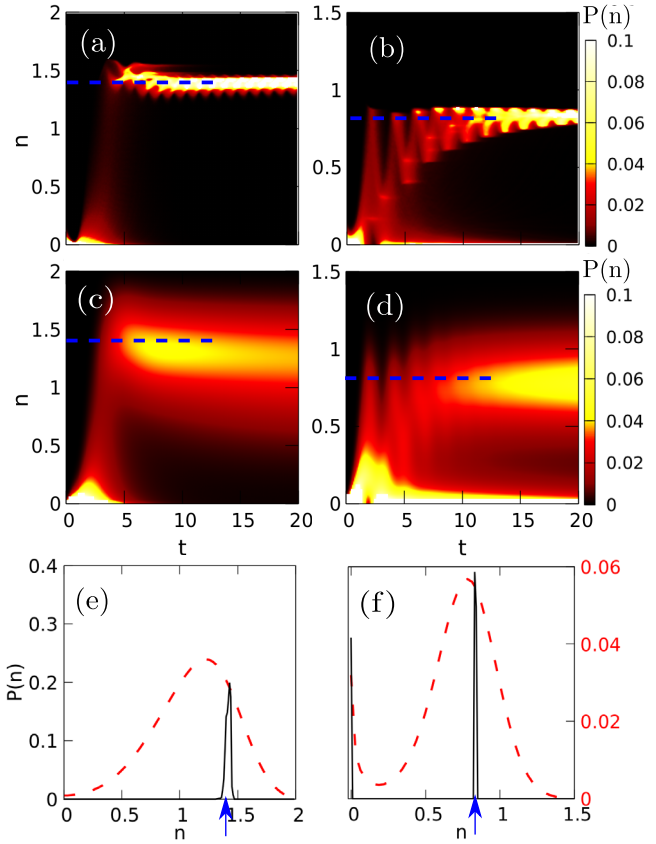

FIG. 3. Relaxation toward NS/SR attractors. we start with all the atoms in the ground state, while $n \sim 0$. (a),(c),(e) $\tilde{g}/g = 0.75$, and the relaxation is toward the SR state. (b),(d),(f) $\tilde{g}/g = 0.48$, and the relaxation is toward NS-SR bistability. The other parameters are $g = 2$, $\kappa = 2$, $\gamma_c = 0.5$, and $f_c = 0.04$. In the quantum simulation, we have $N = 16$ atoms (meaning $\ell = 8$) and use $N_b = 80$ truncation for the bosonic mode. The semiclassical results of (a),(b) and the quantum results of (c),(d) are compared in (e),(f). The waiting time up to the measurement is $t = t_m = 20$. The solid black line is the semiclassical distribution, while the dashed red line is the quantum distribution. The classical SR fixed points are marked by horizontal dashed lines in (a)–(d) and by arrowheads in (e),(f). Note the $n = 0$ peak at (f).

NS to a saddle point is accompanied by the appearance of a pair of broken symmetry $n \neq 0$ SR minima. These two SR states remain attractors provided κ is not too large. For quantitative details, including a $(\kappa, \tilde{g}/g)$ regime diagram, see the Supplemental Material [20] and Fig. 2(b).

Relaxation toward bistability.—In Fig. 3 we inspect the distribution $P(n)$ of the cavity mode's occupation. In the quantum simulation, we start with all the atoms in the ground state, while $n \sim 0$. In the semiclassical simulation, we prepare an initial cloud centered near the south pole of the Bloch sphere $s_z \sim -1/2$, with photon number $n \sim 0$, and let the cloud relax. We compare the outcome of relaxation toward a SR steady state to the relaxation in the bistable NS + SR phase. In the latter case, $P(n)$ exhibits two distinct peaks that exhibit broadening in the quantum simulation. The quantum SR/NS peak ratio is tilted toward the NS with respect to the classical one due to the quantum spilling from the metastable SR state. It is important to realize that this broadening and peak-ratio tilting are not a signature of true quantum interference: similar broadening would have been captured semiclassically, if Langevin noise terms were included [21]. By contrast, the quantum-interference signature we seek cannot be captured by means of stochastic semiclassical simulations.

Quench from chaos.—Having gathered all the necessary ingredients, we turn to discuss the full scenario, including a preparation stage and a quench stage. The purpose of the measurement is to detect chaos in the preparation stage. The quench is to a bistable phase in order to amplify small fluctuations in the prepared state.

The preparation of the chaotic state is demonstrated in Fig. 4. Figure 4(a) demonstrates qualitatively the rather good correspondence that we have between the quantum distribution and the semiclassical cloud. The points are color coded according to which basin they belong: upon quench the blue points will reach the NS fixed point, while the red and magenta points will reach the two SR fixed points. The phase-space location of the basins is better resolved in the Poincaré section of Fig. 4(b).

The *quench* is an abrupt change in the model parameters. Specifically, we force the system to relax toward bistability by setting the parameters $(g, \tilde{g}, \kappa, \gamma_c, f_c)$ to the values specified for Fig. 3(b). This is followed by a wait time

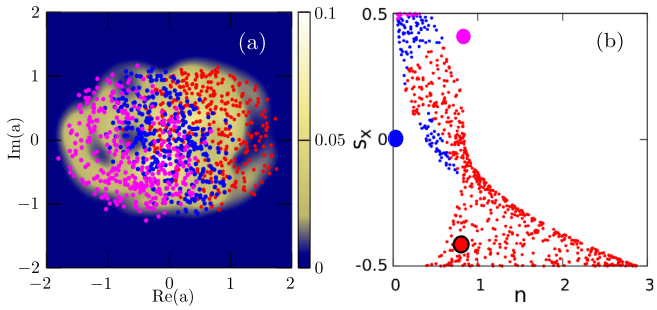

FIG. 4. The prepared state. The system is prepared in a nondissipative chaotic state with $g = 1$ and $\tilde{g} = 0.48$. This is done by launching a coherent state with $s_z = s_x = 1/\sqrt{8}$, and $s_y = 0$, while $n \approx 0$, followed by a long waiting time $50 < t_{\text{prep}} < 1000$. In the quantum simulation, we have $N = 16$ atoms (meaning $\ell = 8$) and use $N_b = 80$ truncation for the bosonic mode. (a) The quantum Husimi distribution of the prepared state in the $[\text{Re}(a) - \text{Im}(a)]$ plane at $t = t_{\text{prep}} = 50$. On top we display the corresponding cloud of classical points. The latter are color coded based on the postquench outcome: blue for those that belong to the NS basin and red and magenta for those of the SR basins. (b) The associated $s_z = 0$ Poincaré section (the $s_y, a > 0$ branch) projected on the $(n - s_x)$ plane, with added blue, red, and magenta circles that indicate the attractors. For the quench we assumed $g = 2$, but kept the same $\tilde{g}/g$, with dissipation parameters $\kappa = 2$ and $\gamma_c = 0.5$ and with incoherent pumping $f_c = 0.04$.

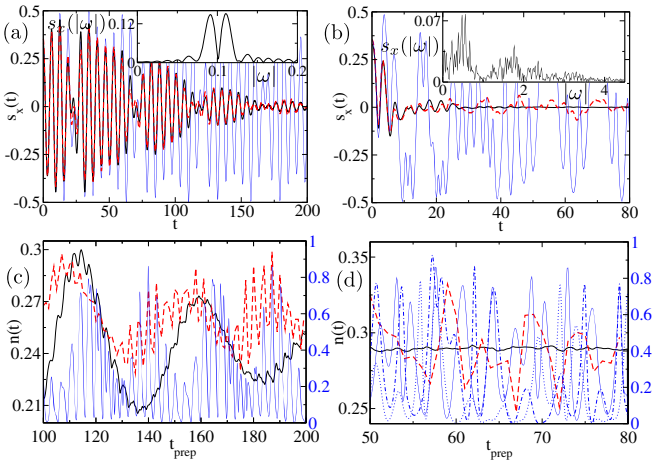

FIG. 5. QFC contrasted with nonchaotic dependence. The outcome of a quench versus the control parameter t_{prep}. The preparation assumes dissipation-free dynamics. (a),(c) For a quench from a $g = 0.1$ quasiregular; (b),(d) for a quench from $g = 1$ chaos. (a),(b) The prequench dynamics of $s_x(t)$. The inset displays the associated classical power spectrum (function of $|\omega|$). (c),(d) The dependence of the quench outcome on t_{prep}. The quench parameters are the same as in Fig. 3, with measurement time $t_m = 2$. Solid blue and black lines are the classical and semiclassical, respectively, while the dashed red line is the quantum. (d) The fluctuations that were caricatured in Fig. 1. The solid, dotted, and dash-dotted blue lines in (d) are representative trajectories of the semiclassical cloud in Fig. 4(a) exhibiting uncorrelated fluctuations.

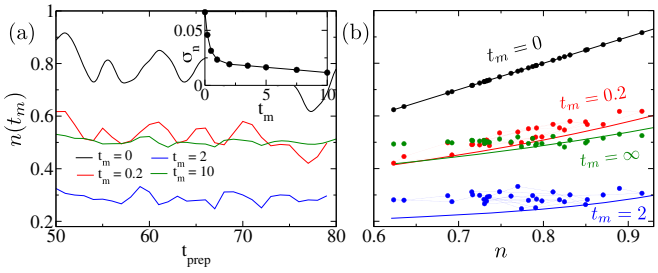

FIG. 6. Suppression of quantum fluctuations. (a) The dependence of $\langle n(t_m)\rangle$ on the control parameter t_{prep} for several values of t_m. For $t_m = 0$ it is merely the conventional calculation of $\langle n\rangle$ versus t for the dissipation-free system. For $t_m = \infty$ (in practice, $t_m = 10$) it is formally a measurement of the final equilibrium state. The intermediate value $t_m = 2$, which has been used in Fig. 5, reflects the outcome of a realistic measurement protocol. It exhibits the fluctuations that were caricatured in Fig. 1. The inset shows the variance σ_n of those fluctuations versus t_m. The partial correlation between $\langle n(t_m)\rangle$ and $\langle n\rangle$ is inspected in (b), where the data points (symbols) of (a) are connected by thin lines. The thick lines are based on a semiclassical procedure that is explained in the main text. The departure of the data points from the latter is due to relaxation.

t_m, during which the system evolves under the dissipative dynamics with the new parameters. At the end of the waiting time, a measurement of $Q = \hat{n}(t_m)$ is preformed. Zero quench time ($t_m = 0$) formally means that there is no quench process, and accordingly, the observable is $Q = \hat{n}(0) = \hat{n}$.

For sufficiently large t_m, disregarding the quantum-noisy broadening effect, the measured quantity is a sum of a projector on the NS basin and a projector on the SR basin, weighted by $n_{\mathrm{NS}} = 0$ and $n_{\mathrm{SR}} \neq 0$,

$$Q = \hat{n}(\infty) = \sum_{r\in \mathrm{NS}} |r\rangle n_{\mathrm{NS}} \langle r| + \sum_{r\in \mathrm{SR}} |r\rangle n_{\mathrm{SR}} \langle r|. \qquad (4)$$

Figure 5 contrasts the outcome of a QFC with the outcome of a quench from quasiperiodic regular dynamics. The time to measurement is intermediate ($t_m = 2$). We clearly see that chaos is reflected in the outcome of the QFC scenario, in accordance with the discussion of Fig. 1. In contrast, the fluctuation due to quench from a regular state is nonerratic and merely reflects the spectral context of the quasiregular dynamics.

Memory loss.—In a mesoscopic device, the information is eventually blurred due to noisy hopping between the fixed points. The outcome of the measurement is presented in Fig. 6(a) for several choices of t_m. We observe memory loss gradually with increasing t_m. For short t_m the systematic variation of Q as a function of t_{prep} is apparent. Furthermore, due to our choice of observable, the outcome is partially correlated with the $t_m = 0$ measurement of $\langle n\rangle$. This is demonstrated in Fig. 6(b). We would like to provide a semiclassical procedure for the analysis of this correlation.

In the semiclassical simulation, the ergodized cloud does not show any fluctuations, and therefore, the postquench dynamics does not depend on the preparation time. However, we can *mimic* the quantum fluctuations by giving each "point" of the semiclassical cloud a weight $w_j \propto (1 + Cn_j)$, where the proportionality constant is determined such that $\sum w_j = 1$. Using the semiclassical equations of motion, we can determine the mapping $n_j \mapsto n_j(t_m)$. Then we can calculate

$$\langle Q\rangle = \langle n(t_m)\rangle_{sc} = \sum_j w_j n_i(t_m). \qquad (5)$$

For each t_{prep} the parameter C is adjusted such that $\langle n(0)\rangle_{sc} = \langle n\rangle_{qm}$. Then we can predict the outcome for finite t_m. The result of this phenomenological theory is incorporated in Fig. 6(b). The departure of the symbols from the calculated lines (e.g., blue as opposed to red symbols) is the signature that fluctuations over the Q of Eq. (4) do not reflect trivially fluctuations of n. On the other hand, the memory loss due to noisy hopping between the fixed points is reflected by the "flattening" of the outcome (e.g., green symbols).

Discussion.—A realistic measurement, unlike an idealized projective measurement, involves a dissipative quench

process. In a macroscopic reality a tossed coin, or a ferromagnetic pointer, will always point "up" or "down" at the end of the quench. For a nonviolent quench, a relatively large t_m is required in order to reach the attractor, allowing differentiation between initially similar states. Thermal and quantum fluctuations can be ignored. But in a mesoscopic context, the time of the quench (t_m) should be optimized in order to keep the information about the measured (prequench) state (it should be large, but not too large). Our emphasis was on QFC, looking for the quantum signature of chaos and clarifying the physical significance of t_m. Per our construction, the "large" t_m measurement was strongly correlated with the $t_m = 0$ measurement, but clearly this is not a general feature. In general, the "basins" of Q are not correlated with a simple observable of the system. Either way, we have demonstrated the manifestation of irregular quantum fluctuations in the outcome, providing signature for chaos in the "measured" state. These fluctuations resemble CAT and UCFs. They are completely diminished in the semiclassical picture and come instead of the classical exponential sensitivity that one would expect if reality were not quantum mechanical. However, unlike UCFs and CAT, they are endangered by memory loss due to relaxation.

This research was supported by the Israel Science Foundation (Grant No. 283/18). S. R. acknowledges a scholarship of the Alexander von Humboldt Foundation, Germany.

[1] P. A. Lee and A. D. Stone, Universal Conductance Fluctuations in Metals, Phys. Rev. Lett. **55**, 1622 (1985).
[2] R. A. Jalabert, Mesoscopic transport and quantum chaos, Scholarpedia, **11**, 30946 (2016).
[3] S. Tomsovic and D. Ullmo, Chaos-assisted tunneling, Phys. Rev. E **50**, 145 (1994).
[4] H. Ritsch, P. Domokos, F. Brennecke, and T. Esslinger, Cold atoms in cavity-generated dynamical optical potentials, Rev. Mod. Phys. **85**, 553 (2013).
[5] P. Kirton, M. M. Roses, J. Keeling, and E. G. Dalla Torre, Introduction to the Dicke model: From equilibrium to nonequilibrium, and vice versa, Adv. Quantum Technol. **2**, 1970013 (2019).
[6] S. Genway, W. Li, C. Ates, B. P. Lanyon, and I. Lesanovsky, Generalized Dicke Nonequilibrium Dynamics in Trapped Ions, Phys. Rev. Lett. **112**, 023603 (2014).
[7] P. Kirton and J. Keeling, Superradiant and lasing states in driven-dissipative Dicke models, New J. Phys. **20**, 015009 (2018).
[8] K. C. Stitely, A. Giraldo, B. Krauskopf, and S. Parkins, Nonlinear semiclassical dynamics of the unbalanced, open Dicke model, Phys. Rev. Research **2**, 033131 (2020).
[9] N. Shammah, S. Ahmed, N. Lambert, S. De Liberato, and F. Nori, Open quantum systems with local and collective incoherent processes: Efficient numerical simulations using permutational invariance, Phys. Rev. A **98**, 063815 (2018).
[10] D. Meiser and M. J. Holland, Steady-state superradiance with alkaline-earth-metal atoms, Phys. Rev. A **81**, 033847 (2010).
[11] Z. Zhiqiang, C. H. Lee, R. Kumar, K. J. Arnold, S. J. Masson, A. S. Parkins, and M. D. Barrett, Nonequilibrium phase transition in a spin-1 Dicke model, Optica **4**, 424 (2017).
[12] J. G. Bohnet, Z. Chen, J. M. Weiner, D. Meiser, M. J. Holland, and J. K. Thompson, A steady-state superradiant laser with less than one intracavity photon, Nature (London) **484**, 78 (2012).
[13] R. H. Dicke, Coherence in spontaneous radiation processes, Phys. Rev. **93**, 99 (1954).
[14] C. Emary and T. Brandes, Quantum Chaos Triggered by Precursors of a Quantum Phase Transition: The Dicke Model, Phys. Rev. Lett. **90**, 044101 (2003).
[15] L. Bakemeier, A. Alvermann, and H. Fehske, Dynamics of the Dicke model close to the classical limit, Phys. Rev. A **88**, 043835 (2013).
[16] K. Baumann, C. Guerlin, F. Brennecke, and T. Esslinger, Dicke quantum phase transition with a superfluid gas in an optical cavity, Nature (London) **464**, 1301 (2010).
[17] J. Klinder, H. Keßler, M. R. Bakhtiari, M. Thorwart, and A. Hemmerich, Observation of a Superradiant Mott Insulator in the Dicke-Hubbard Model, Phys. Rev. Lett. **115**, 230403 (2015).
[18] M. A. Bastarrachea-Magnani, S. Lerma-Hernández, and J. G. Hirsch, Comparative quantum and semiclassical analysis of atom-field systems. I. Density of states and excited-state quantum phase transitions, Phys. Rev. A **89**, 032101 (2014).
[19] M. A. Bastarrachea-Magnani, S. Lerma-Hernández, and J. G. Hirsch, Comparative quantum and semiclassical analysis of atom-field systems. II. Chaos and regularity, Phys. Rev. A **89**, 032102 (2014).
[20] See Supplemental Material at http://link.aps.org/supplemental/10.1103/PhysRevLett.128.130604 for details on the stability analysis and the phase diagrams; borders of the NS and SR regions; the bistability region; the regular and the chaotic lasing regions; and the comparison of QFC to a quench from regular dynamics.
[21] C. Gardiner and P. Zoller, *Quantum Noise: A Handbook of Markovian and Non-Markovian Quantum Stochastic Methods with Applications to Quantum Optics* (Springer Science, New York, 2004).